Establishing Age-Associated Normative Ranges of the Cerebral ^{18}F-FDG Uptake Ratio in Children

Chiaho Hua[1], Thomas E. Merchant[1], Xingyu Li[2], Yimei Li[2], and Barry L. Shulkin[1]

[1]*Department of Radiological Sciences, St. Jude Children's Research Hospital, Memphis, Tennessee; and* [2]*Department of Biostatistics, St. Jude Children's Research Hospital, Memphis, Tennessee*

In this study, we reported age-associated ranges of the regional cerebral ^{18}F-FDG uptake ratio in pediatric patients as a surrogate to normative data from healthy children. **Methods:** ^{18}F-FDG PET scans of 132 children and adolescents (age, 1−20 y) with non–central nervous system–related diseases and normal-appearing tracer distributions in the brain were retrospectively analyzed. PET images of individual patients were warped to a 3-dimensional reference template. Uptake ratio was calculated for 63 anatomic regions by normalizing the regional count per voxel with the average count per voxel in all regions. Models of regional uptake ratio as a function of age and sex were developed to calculate the 95% prediction interval. **Results:** The paracentral lobule and cuneus had the highest resting metabolic state among all gray matter regions, whereas the brain stem, uncus, and hippocampus had the lowest uptake. A large left–right asymmetry was present in the angular gyrus and inferior occipital gyrus. Quantitative data of the regression, 95% confidence interval, and 95% prediction interval for each age were summarized for the 63 regions. In 52 of 63 regions, the ^{18}F-FDG uptake ratio had a significant age effect. The linear model was optimal for 12 regions, whereas the spline model with 1 age knot was a better fit for 40 regions. In children younger than 5 y, frontal and temporal lobes had a lower uptake than parietal and occipital lobes in general. However, uptake in the frontal lobe continued to increase with age but it decreased in the parietal and occipital lobes. **Conclusion:** Anatomic regions of the brain in children and adolescents exhibited uniquely different ^{18}F-FDG uptake trends with age. Our results may be useful for studying childhood development and possibly regional metabolic defects in children with traumatic brain injury or central nervous system disorders or children receiving cancer treatment.

Key Words: PET; ^{18}F-FDG; children; brain

J Nucl Med 2015; 56:575–579
DOI: 10.2967/jnumed.114.146993

The establishment of an age-associated normative range of cerebral ^{18}F-FDG uptake in children and adolescents is important in many applications. This parameter helps us understand the normal developmental trajectories of different regions in a child's brain and complements findings from studies on anatomic imaging, neurologic function, and cognitive and behavioral development. In children who have brain defects due to diseases, traumatic injury, or cancer treatment, individual PET studies can be compared with this normative benchmark to identify abnormal metabolic regions that can be targeted for subsequent intervention. However, there are few studies on the normative pattern of ^{18}F-FDG uptake in children (*1–6*). Because of the few pediatric PET scans obtained at most hospitals, previous studies were limited to small numbers of subjects, focused only on selected regions, or did not cover a wide age range.

We conducted a retrospective study to determine the age-associated ranges of the regional cerebral ^{18}F-FDG uptake ratio in a large cohort of pediatric patients with non–central nervous system (CNS) diseases as a surrogate to normative data from healthy children. Our reporting of the self-normalized regional uptake ratio rather than the absolute metabolic rate makes it straightforward for other institutions to compare as arterial blood sampling in dynamic scans is not practical in children. Although we did not adopt absolute rate, the use of uptake ratio was inherently quantitative. To alleviate the problem that absolute standardized uptake value is subject to many sources of variability (*7*), we performed the self-normalization on the basis of the average ^{18}F-FDG uptake by all brain regions and found it superior to the conventional approach that uses the cerebellum as a reference region.

MATERIALS AND METHODS

Study Population

Acquired between August 2011 and July 2013, ^{18}F-FDG PET scans of 132 consecutive children and adolescents with non-CNS–related diseases were analyzed in an institutional review board–approved retrospective study. The need for written informed consent was waived. One PET dataset was used for each child. Figure 1 shows the age distribution of the 132 children (68 males and 64 females; median age, 13 y; age range, 1−20 y). Age was truncated to an integer. Diagnoses included Hodgkin lymphoma (n = 33), non-Hodgkin lymphoma (n = 20), osteosarcoma (n = 10), Ewing sarcoma (n = 8), melanoma (n = 5), and other tumor types (n = 56). Patients did not receive surgery or other invasive procedures to the brain and did not have a history of mental disability before PET scanning. All scans were obtained before the administration of any systemic chemotherapy or anticancer drugs. An experienced nuclear medicine physician reviewed the scans to ensure that the cerebral uptake distributions appeared normal.

PET Image Acquisition

Whole-body ^{18}F-FDG PET studies were performed on patients who fasted overnight or for at least 4 h before the afternoon scan. Blood glucose levels were checked before the injection to ensure that they were below 120 mg/dL. ^{18}F-FDG at 5.55 MBq/kg of body weight (minimum, 74-MBq dose; maximum, 444-MBq dose) was

Received Sep. 8, 2014; revision accepted Jan. 19, 2015.
For correspondence contact: Chiaho Hua, Department of Radiological Sciences, St. Jude Children's Research Hospital, Mail Stop 220, 262 Danny Thomas Place, Memphis, TN 38105-3678.
E-mail: chia-ho.hua@stjude.org
Published online Mar. 5, 2015.

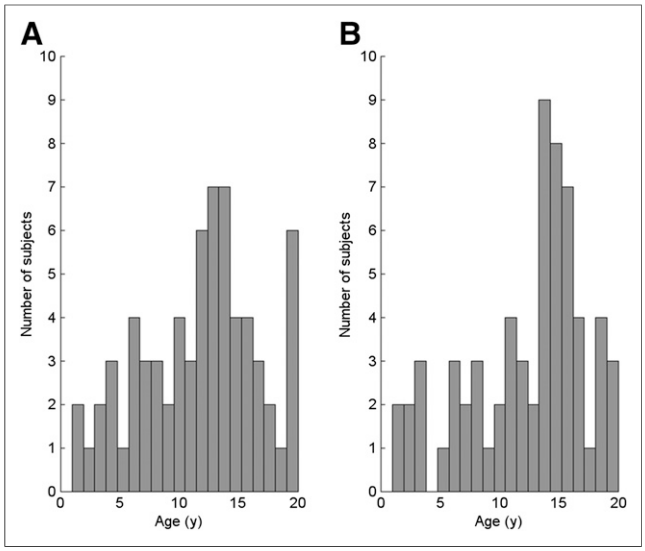

FIGURE 1. Age distribution of 132 patients in study: 68 males (A) and 64 females (B).

administered 1 h before the start of imaging. For patients younger than 7 y, anesthesia was not initiated until the time of scanning. A transmission CT scan for attenuation correction was acquired, followed by emission imaging at multiple bed positions in the 3-dimensional (3D) mode for 3–5 min per bed position, using a Discovery 690 PET/CT system (GE Healthcare). Non–time-of-flight attenuation-corrected PET images were iteratively reconstructed by standard vendor-provided software, using a voxel size of 3.65 × 3.65 × 3.27 mm.

Data Analysis

The brain section from the vertex to the skull base was separated from the whole-body PET images and then processed. PET images of each patient were first linearly registered (9-parameter affine transformation) and then nonlinearly warped to a 3D reference template of ^{18}F-FDG PET in Talairach coordinates using the HERMES Brain Analysis software (version 3.5; Hermes Medical Solutions). In the unlikely event of fit needing adjustments, fit parameters can be fine-tuned to achieve a better match of isocontour of the template overlaid. Implementation of the algorithm and its applications were published earlier (*8–13*). Predefined regions of interest for 63 cerebral regions were overlaid on the spatially normalized images to calculate the total count and the count per voxel (Fig. 2). To facilitate comparison across patients without the limitations of absolute standardized uptake value, the count per voxel in each cerebral region was divided by the average count per voxel in all regions. For simplicity, this measure is hereafter designated the regional uptake ratio, which is similar to the concept of standardized uptake value ratio. The list of anatomic regions has been previously summarized (*12*) and consists of cortical (gyri in frontal, temporal, parietal, and occipital lobes) and subcortical structures (limbic system, basal ganglia, thalamus, cerebellum, and brain stem).

All statistical analyses were performed using the computing environment R, version 3.0.1 (R-Project.org) (*14*). The objective was to model the regional uptake ratio as a function of age. Scatter plots of the regional uptake ratio versus age for all patients, smoothed by a local regression technique (*15*), were examined for general trends. According to the trend observed, raw data were fitted with all possible models using linear, quadratic, and spline (piecewise linear) equations. The sex term was added to models for fitting if the 2-sample *t* test result was significant ($P < 0.05$). The following are examples of models wherein both sex and age effects were significant.

$$\text{Linear: regional uptake ratio} = \beta_0 + \beta_1 \times \text{age} + \beta_2 \times \text{gender}$$

$$\text{Quadratic: regional uptake ratio} = \beta_0 + \beta_1 \times \text{age} + \beta_2 \times \text{age}^2 + \beta_3 \times \text{gender}$$

$$\text{Spline: regional uptake ratio} = \beta_0 + \beta_1 \times \text{age} + \beta_2 \times \text{gender} + \beta_3 \times (\text{age} - \text{knot})_+$$

$$\text{where } (\text{age} - \text{knot})_+ = \begin{cases} \text{age} - \text{knot} & \text{if } (\text{age} - \text{knot}) > 0 \\ 0 & \text{otherwise} \end{cases}$$

$$\text{and gender} = \begin{cases} 0 & \text{if gender} = \text{female} \\ 1 & \text{if gender} = \text{male} \end{cases}$$

where knot denotes a cut point splitting the age axis into age groups and β_0, β_1, and β_2 are fitting coefficients. The optimal model was chosen if it had the smallest Akaike information criterion and the smallest prediction mean square error. For each region, the predicted uptake ratio, 95% confidence interval for the predicted value, and 95% prediction interval were calculated at each age from 1 to 20 y.

RESULTS

Interregional Variations in ^{18}F-FDG Uptake

The distributions of the uptake ratio calculated for 63 anatomic regions by combining all ages in the 132 patients are shown in Supplemental Figure 1 (supplemental materials are available at http://jnm.snmjournals.org). The paracentral lobule and cuneus had the highest average uptake among all gray matter regions, which was 15% higher than the average uptake of all regions. The brain stem, uncus, and hippocampus had the lowest uptake, which was approximately 30% lower than the average. The inferior occipital gyrus and medial occipitotemporal gyrus had the largest variation in uptake across patients, followed by the cerebellum and caudate nucleus. In these regions, the variability was largely intrinsic and to a lesser degree caused by the age-associated changes because their age-specific 95% prediction intervals were also the largest (0.25–0.38), as can be seen in Supplemental Figure 2 and Supplemental Table 2. There was a larger left–right asymmetry in the inferior occipital gyrus and angular gyrus, with the left higher than the right region.

Model Fitting and Age-Related Trends

Figure 3 shows the distribution of regional uptake ratio versus age and the model fit for selected anatomic regions (Supplemental Fig. 2 for all 63 regions and Supplemental Fig. 3 for the same *y*-axis scale). Supplemental Table 1 lists the age association, the optimal regression model for each region, and the age range in which the uptake ratio was significantly associated. Supplemental Table 2 summarizes the age-corresponding predicted value and lower and upper bounds of 95% and 99% prediction intervals of all regions. The uptake ratio in 52 of 63 regions was significantly associated with age. For the remaining 11 regions, the fits were relatively constant with age. When age was not a significant factor, no model was built. The mean value, rather than the optimal model fitted value, was used as the predicted value. The sex effect was present in 5 regions only, and the distributions for males and females were

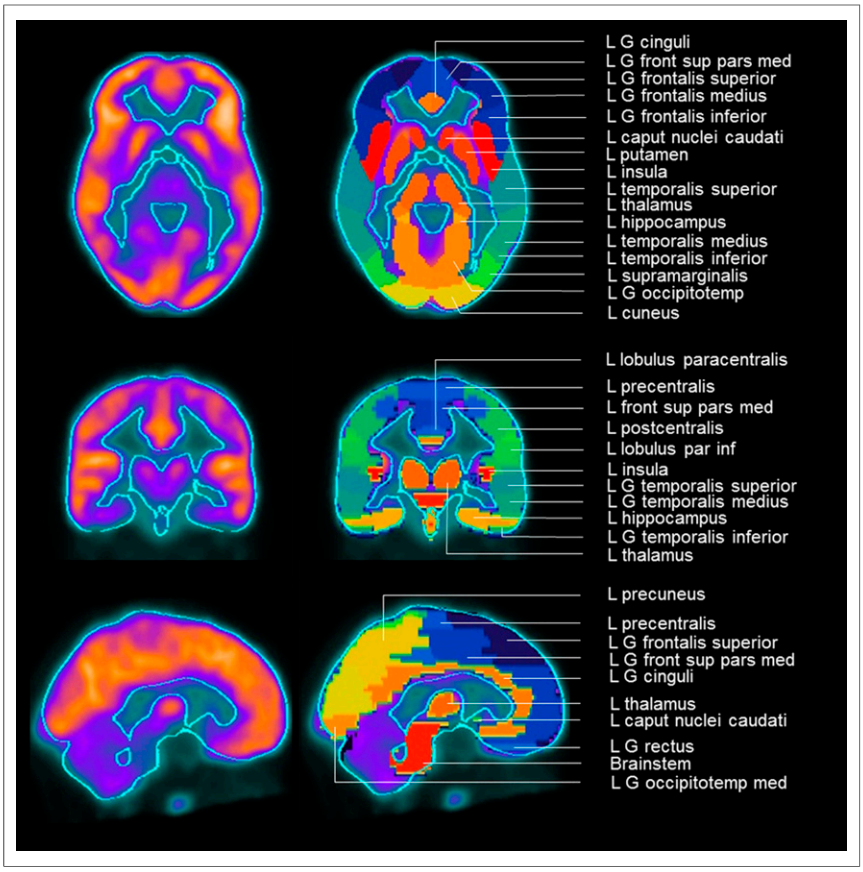

FIGURE 2. Spatially normalized ^{18}F-FDG PET (left) and region-of-interest overlays (right) of example patient. front = frontalis; G = gyrus; inf = inferior; med = medial; occipitotemp = occipitotemporalis; par = parietalis; sup = superior.

plotted separately in these cases. The uptake ratios in 10 regions were not associated with age or sex.

The linear model was the optimal model for 12 regions, whereas the spline model with 1 age knot was a better fit for 39 regions. Only 1 region (right insula) had similar Akaike information criterion and prediction mean square error for spline and quadratic models. Its spline model was reported. For the spline models, age knots varied from 4 to 16 y (median, 10 y). In general, the fitted time trend either linearly increased at a younger age and then linearly decreased or vice versa. However, in 26 of 40 regions this effect of age was only significant before or after the age knot.

Relative Changes in Uptake Ratio with Age in Different Lobes

Figure 4 shows the relative changes in ^{18}F-FDG uptake in different lobes of the brain. In children younger than 5 y, the parietal and occipital lobes had relatively higher uptake than did frontal and temporal lobes. However, uptake ratios of the parietal and occipital lobes decreased with age, whereas those of the frontal lobe increased and then declined. Temporal lobes had the lowest uptake throughout the entire age range. Notably, the gyrus rectus and gyrus orbitalis of the frontal lobe had a lower uptake than other regions (Supplemental Fig. 1) and did not share the same time trend as that of other frontal lobe regions (Supplemental Fig. 2).

DISCUSSION

The purpose of our study was to fit data on cerebral ^{18}F-FDG uptake from a large cohort of children and provide age-associated ranges that can be used to guide future childhood development and brain dysfunction studies. To our knowledge, this is the largest number of ^{18}F-FDG PET scans of pediatric patients and regions of interest analyzed to date.

Previous studies of normal cerebral uptake of ^{18}F-FDG in children reported that regions of the brain responsible for more basic functions mature earlier than those involved in high-order functions (*4,16*). In early childhood, parietal and occipital lobes have a higher uptake than other lobes; however, the frontal lobe has a more rapid increasing trend in uptake and eventually exceeds the uptake of the parietal and occipital lobes (*5,6*). A recent report of voxel-based ^{18}F-FDG uptake analysis using statistical parametric mapping also showed increasing uptake with age in the premotor and prefrontal cortices (*17*). The metabolic rates of the frontal cortex start declining after reaching the maximum (*18*). The temporal lobe has the lowest metabolic rate among the major cerebral lobes from early life into adulthood (*1*). Our results (Fig. 4; Supplemental Fig. 2) are consistent with these general observations. However, our study showed that some regions in the parietal and occipital lobes (e.g., the cuneus in the occipital lobe and paracentral lobule and the precuneus in the parietal lobe) were still consistently among those with the highest uptake from early childhood to young adulthood.

Our data in the frontal lobe showed that the uptake ratios in superior, medial, and inferior frontal gyri peaked in the second decade of life, with the superior frontal gyrus being the latest (age knots, 13−14 y in the spline models). This late peaking may reflect the fact that the prefrontal cortex, especially the dorsolateral prefrontal region, has a protracted neural and functional maturation, compared with other cerebral lobes (*19–21*), and an accelerated gray matter density loss from adolescence to adulthood despite continued brain growth (*22*). A similar time trend was also observed in 2 major areas with earlier peak ages (5−10 y): superior and middle temporal gyri and inferior parietal lobule containing angular and supramarginal gyri. This trend may be related to the fact that the primary auditory cortex matures early and stabilizes by age 7 y (*23*). The other regions associated with higher-order language skills continue to mature, involving dendritic pruning into adolescence. Decreasing regional cerebral blood flow with age has been observed (*23,24*).

Pediatric PET data could contribute to the understanding of maturation of brain functional networks, which was often studied with resting-state functional MR imaging, diffusion tensor imaging, perfusion imaging, anatomic MR imaging, and electroencephalography (*25,26*). Recent studies have demonstrated that homotopic intersubject metabolic covariances observed using PET were comparable to the corresponding resting-state functional MR imaging time series correlations (*27*), and the pattern of elevated local neural activity

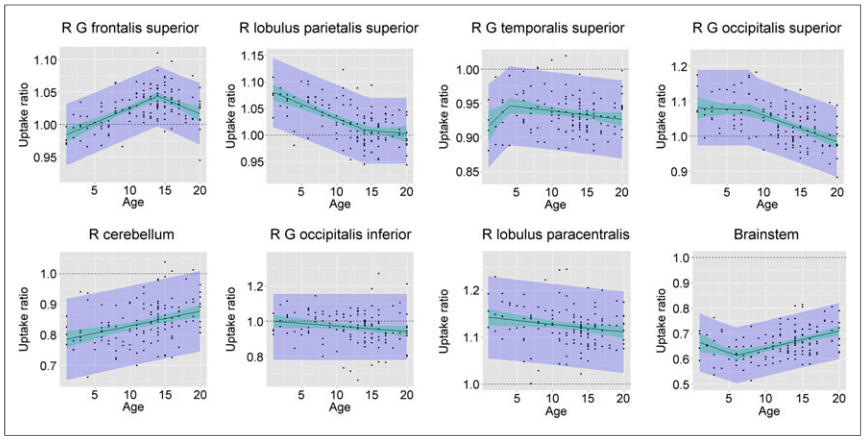

FIGURE 3. Distributions of ^{18}F-FDG uptake ratio versus age (in y) in selected anatomic regions. Each dot represents a patient. Solid line in middle of each plot represents fitted regression model, green shaded area around line represents 95% confidence interval for fitted regression model, and purple shaded area represents 95% prediction interval. G = gyrus.

from ^{18}F-FDG PET coincided with the pattern of functional connectivity measured with resting-state functional MR imaging when both images were simultaneously acquired (*28*). The quantitative data provided by this study can be further exploited to extract age-associated differences in interregional patterns of functional connectivity for comparison with findings from other neuroimaging modalities.

For intrasubject normalization, we used the average count per voxel in all regions instead of the cerebellum as the reference region. The use of cerebellar uptake for self-normalization has been cautioned because reduced cerebellar metabolism often occurs in patients with stroke or brain tumors (*29–31*). We have also observed this phenomenon in a separate cohort of pediatric brain tumor patients (unpublished data). Although reduced cerebellar metabolism may not occur in healthy children, it could lead to error in the case of children with brain tumors when the same normalization scheme is applied for comparison with our reported data. In addition, the age-specific variation in regional uptake ratio across subjects appeared to be larger and the age trend less clear with the cerebellar normalization method than for the average uptake in all regions for self-normalization (Supplemental Fig. 4). Our findings suggest that the use of average uptake in the brain for self-normalization may be more advantageous. There is a caveat when performing this type of normalization on patients whose regional changes in ^{18}F-FDG uptake significantly affect the whole-brain mean in the same direction, for example, extensive cerebral hypometabolism. In this scenario, the whole-brain mean would become much lower and the uptake ratios of abnormal regions could be underestimated if the regional changes were greater than the whole-brain changes or, in the most extreme case, did not appear abnormal with the smaller regions of retained uptake being erroneously detected as showing an abnormally increased uptake ratio.

One limitation of our study was the use of pediatric patients with extracranial diseases and normal-appearing ^{18}F-FDG distribution of the brain as a surrogate to healthy children. In addition, because of the limited availability of dedicated brain scans in children who did not have CNS diseases, brain sections of whole-body PET scans were used instead to calculate the regional cerebral uptake ratios. Whole-body PET scans had a larger pixel spacing than did routine dedicated PET scans of the brain (3.65 vs. 1.56 mm), whereas the slice thickness for both types of scans was the same (3.27 mm). The dedicated brain scan was acquired in 3D mode for 8 min. The brain portion of the whole-body PET was acquired in 3D for 3–5 min as was each body position of the torso. However, comparison of data from 5 patients (2−16 y; median, 5 y) who underwent both dedicated brain and whole-body PET scans in the same imaging session revealed that the average difference in uptake ratio ([whole-body uptake ratio − dedicated brain uptake ratio]/dedicated brain uptake ratio) for all regions between both types of scans was only 0.33%, with almost all regions less than ±2% difference. The gyrus rectus, gyrus orbitalis, insula, and brain stem had a 2%−6% higher uptake ratio in the whole-body PET scan than the brain PET scan. One explanation for this observation is that this small increase is due to the timing of image acquisition. When both dedicated brain and whole-body ^{18}F-FDG PET scans are obtained in a single session, the dedicated brain acquisition precedes the whole-body study. Thus, it is possible that those structures that have higher uptake in the brain on whole-body ^{18}F-FDG

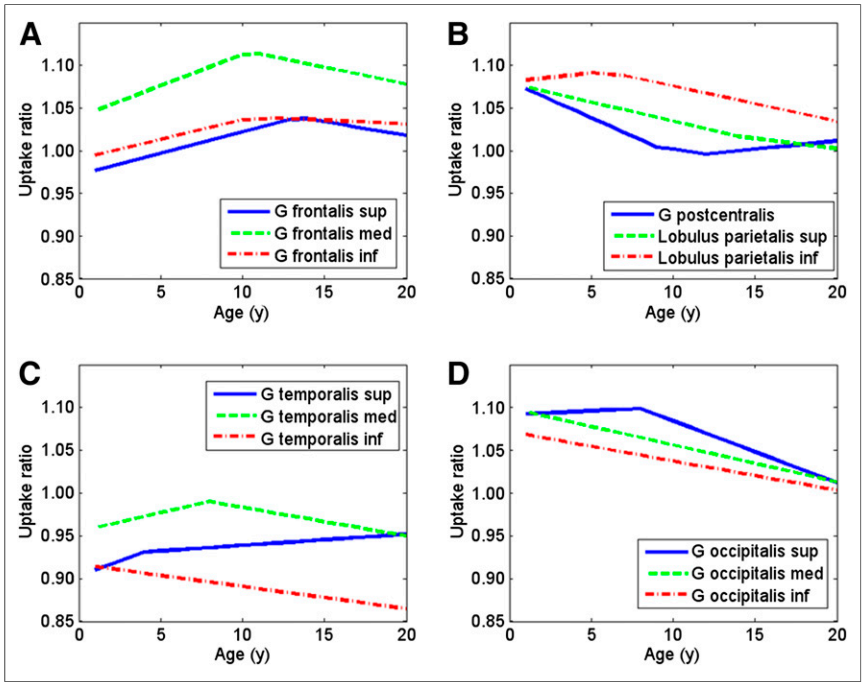

FIGURE 4. Relative changes of uptake ratio with age in frontal (A), parietal (B), temporal (C), and occipital (D) lobes of brain. Ratios of right and left regions were averaged to produce plot. G = gyrus; inf = inferior; med = medial; sup = superior.

PET scans than on dedicated ^{18}F-FDG PET brain scans continue to accumulate ^{18}F-FDG during the image acquisition of the dedicated brain ^{18}F-FDG PET and during the time required to prepare the whole-body scan. Dynamic ^{18}F-FDG PET studies of the brain would be required for detailed exploration of this hypothesis, but this could be impractical in a clinical setting. Nevertheless, more subjects are needed to better confirm their equivalence or derive region-specific correction factors before direct comparison.

In our study, the brain warping and segmentation were performed using a single adult-size template of ^{18}F-FDG PET provided by the commercial software. Although a child's brain has reached approximately 95% of its average adult size by age 6 (*32*), there is a concern that the warping for young children could be less accurate. Potential errors in segmenting small structures of young children could lead to a bias in subsequent uptake modeling, although lower spatial resolution of PET is arguably more forgiving than other high-resolution imaging modalities. We relied on visual inspection instead of mathematic assessment to determine whether automatic warping was acceptable. In addition, atlas-based autosegmentation has a major limitation in accuracy when the brain morphology of the test subject deviates significantly from the population used in constructing the atlas (*33*), for example, a large surgical cavity or the presence of a large brain tumor. Thus, caution is warranted when comparing these reported ranges of uptake ratio with young children or patients with severe brain deformation. More advanced segmentation algorithms or simple manual contouring on spatially registered MR imaging by clinical experts may be beneficial in such patients.

CONCLUSION

This study provided age-associated data on ^{18}F-FDG uptake ratios in various anatomic regions of the developing brain. We performed self-normalization using the average brain uptake and fitted data from a large cohort of children and adolescents. Our findings may be useful for studying childhood development and possibly regional metabolic defects in children with traumatic brain injury or CNS disorders or in children receiving cancer treatment.

DISCLOSURE

The costs of publication of this article were defrayed in part by the payment of page charges. Therefore, and solely to indicate this fact, this article is hereby marked "advertisement" in accordance with 18 USC section 1734. No potential conflict of interest relevant to this article was reported.

ACKNOWLEDGMENTS

We thank Tina Davis for data collection and IRB compliance, Lisa Mills for assistance with the PET software, Erika Thompson for secretarial expertise, and Dr. Vani Shanker for scientific editing.

REFERENCES

1. Chugani HT, Phelps ME, Mazziotta JC. Positron emission tomography study of human brain functional development. *Ann Neurol.* 1987;22:487–497.
2. Van Bogaert P, Wikler D, Damhaut P, Szliwowski HB, Goldman S. Regional changes in glucose metabolism during brain development from the age of 6 years. *Neuroimage.* 1998;8:62–68.
3. Kang E, Lee DS, Kang HJ, et al. Age-associated changes of cerebral glucose metabolic activity in both male and female deaf children: parametric analysis using objective volume of interest and voxel-based mapping. *Neuroimage.* 2004;22:1543–1553.
4. Gogtay N, Giedd JN, Lusk L, et al. Dynamic mapping of human cortical development during childhood through early adulthood. *Proc Natl Acad Sci USA.* 2004;101:8174–8179.
5. London K, Howman-Giles R. Normal cerebral FDG uptake during childhood. *Eur J Nucl Med Mol Imaging.* 2014;41:723–735.
6. Shan ZY, Leiker AJ, Onar-Thomas A, et al. Cerebral glucose metabolism on positron emission tomography of children. *Hum Brain Mapp.* 2014;35:2297–2309.
7. Boellaard R. Standards for PET image acquisition and quantitative data analysis. *J Nucl Med.* 2009;50:11S–20S.
8. Studholme C, Hill DLG, Hawkes DJ. An overlap invariant entropy measure of 3D medical image alignment. *Pattern Recognit.* 1999;32:71–86.
9. Slomka PJ, Radau P, Hurwitz GA, Dey D. Automated three-dimensional quantification of myocardial perfusion and brain SPECT. *Comput Med Imaging Graph.* 2001;25:153–164.
10. Radau PE, Slomka PJ, Julin P, Svensson L, Wahlund LO. Evaluation of linear registration algorithms for brain SPECT and the errors due to hypoperfusion lesions. *Med Phys.* 2001;28:1660–1668.
11. Van Laere K, Koole M, D'Asseler Y, et al. Automated stereotactic standardization of brain SPECT receptor data using single-photon transmission images. *J Nucl Med.* 2001;42:361–375.
12. Montandon M-L, Zaidi H. Quantitative analysis of template-based attenuation compensation in 3D brain PET. *Comput Med Imaging Graph.* 2007;31:28–38.
13. Garibotto V, Montandon ML, Viaud CT, et al. Regions of interest-based discriminant of DaTSCAN SPECT and FDG-PET for the classification of dementia. *Clin Nucl Med.* 2013;38:e112–e117.
14. R-Project.org. *R: A Language and Environment for Statistical Computing*. R-Project website. http://www.R-project.org/. Accessed February 23, 2015.
15. Cleveland WS, Loader CL. Smoothing by local regression: principles and methods. In: Haerdle W, Schimek MG, eds. *Statistical Theory and Computational Aspects of Smoothing*. New York, NY: Springer; 1996:10–49.
16. Lenroot RK, Giedd JN. Brain development in children and adolescents: insights from anatomical magnetic resonance imaging. *Neurosci Biobehav Rev.* 2006;30:718–729.
17. London K, Howman-Giles R. Voxel-based analysis of normal cerebral [^{18}F]FDG uptake during childhood using statistical parametric mapping. *Neuroimage.* 2015;106:264–271.
18. Muzik O, Janisse J, Ager J, et al. A mathematical model for the analysis of cross-sectional brain glucose metabolism data in children. *Prog Neuropsychopharmacol Biol Psychiatry.* 1999;23:589–600.
19. Fuster JM. Frontal lobe and cognitive development. *J Neurocytol.* 2002;31:373–385.
20. Conklin HM, Luciana M, Hooper CJ, Yarger RS. Working memory performance in typically developing children and adolescents: behavioral evidence of protracted frontal lobe development. *Dev Neuropsychol.* 2007;31:103–128.
21. Giedd JN, Raznahan A, Lenroot RK. Adolescent frontal lobes: under construction. In: Stuss DT, Knight RT, eds. *Principles of Frontal Lobe Function*. New York, NY: Oxford University Press; 2013:135–144.
22. Sowell ER, Thompson PM, Tessner KD, Toga AW. Mapping continued brain growth and gray matter density reduction in dorsal frontal cortex: inverse relationships during postadolescent brain maturation. *J Neurosci.* 2001;21:8819–8829.
23. Devous MD Sr, Altuna D, Furl N, et al. Maturation of speech and language functional neuroanatomy in pediatric normal controls. *J Speech Lang Hear Res.* 2006;49:856–866.
24. Moore JK. Maturation of human auditory cortex: implications for speech perception. *Ann Otol Rhinol Laryngol Suppl.* 2002;189:7–10.
25. Uddin LQ, Supekar K, Menon V. Typical and atypical development of functional human brain networks: insights from resting-state fMRI. *Front Syst Neurosci.* 2010;4:21.
26. Craddock RC, Jbabdi S, Yan C-G, et al. Imaging human connectomes at the macroscale. *Nat Methods.* 2013;10:524–539.
27. Di X, Biswal BB. Metabolic brain covariant networks as revealed by FDG-PET with reference to resting-state fMRI networks. *Brain Connect.* 2012;2:275–283.
28. Riedl V, Bienkowska K, Strobel C, et al. Local activity determines functional connectivity in the resting human brain: a simultaneous FDG-PET/fMRI study. *J Neurosci.* 2014;34:6260–6266.
29. Kushner M, Tobin M, Alavi A, et al. Cerebellar glucose consumption in normal and pathologic states using fluorine-FDG and PET. *J Nucl Med.* 1987;28:1667–1670.
30. Shamoto H, Chugani HT. Glucose metabolism in the human cerebellum: an analysis of crossed cerebellar diaschisis in children with unilateral cerebral injury. *J Child Neurol.* 1997;12:407–414.
31. Otte A, Roelcke U, von Ammon K, et al. Crossed cerebellar diachisis and brain tumor biochemistry studied with positron emission tomography, [^{18}F]fluoroseoxyglucose and [^{11}C]methionine. *J Neurol Sci.* 1998;156:73–77.
32. Lenroot RK, Gogtay N, Greenstein DK, et al. Sexual dimorphism of brain development trajectories during childhood and adolescence. *Neuroimage.* 2007;36:1065–1073.
33. Shiee N, Bazin PL, Cuzzocreo JL, et al. Segmentation of brain images using adaptive atlases with application to ventriculomegaly. *Inf Process Med Imaging.* 2011;22:1–12.